Chinese Chemical Letters 34 (2023) 108267

Contents lists available at ScienceDirect

Chinese Chemical Letters

journal homepage: www.elsevier.com/locate/cclet

Manipulation and observation of atomic-scale superlattices in perovskite manganate

Xiyang Wang, Keke Huang, Xiaofeng Wu, Long Yuan, Liping Li, Guangshe Li, Shouhua Feng*

State Key Laboratory of Inorganic Synthesis and Preparative Chemistry, College of Chemistry, Jilin Provincial International Cooperation Key Laboratory of Advanced Inorganic Solid Functional Materials, Jilin University, Changchun 130012, China

ARTICLE INFO

Article history:
Received 20 October 2022
Revised 23 February 2023
Accepted 23 February 2023
Available online 27 February 2023

Keywords:
Perovskite oxides
Hydrothermal
Ordered superstructure
Perovskite superlattice
Disproportionation reaction

ABSTRACT

Superlattices in crystals, particularly in perovskite oxides with strong correlation effects, can create new states of matter and produce peculiar physicochemical phenomena. However, the newfangled perovskite superlattices depend on physical deposition with unit-cell precision. It has been challenging to explore a new suitable chemical method to tailor perovskite superlattices. Herein, we present a new bottom-up strategy to precisely prepare atomic-scale oxide superlattices of $(LaMnO_3)_1$-$(La_{1-x-y}Ca_xK_yMnO_3)_2$ in a monodispersed perovskite $La_{0.66}Ca_{0.29}K_{0.05}MnO_3$ (LCKMO). The special atomic-scale perovskite superlattices are demonstrated using SAED, HAADF-STEM, XRD, and atomic-resolution elemental mapping. Our experiments reveal that the perovskite superlattices can be fabricated under extreme hydrothermal conditions utilizing ultra-high concentrations of KOH. An approximate molten salt system in the hydrothermal process can induce the disproportionation reaction of MnO_2 solids, which is vital to the growth of ordered perovskite superlattices. This work not only clarifies the hydrothermal growth process of perovskite oxides in extreme conditions, but also proposes a novel engineering route toward perovskite superlattices.

© 2023 Published by Elsevier B.V. on behalf of Chinese Chemical Society and Institute of Materia Medica, Chinese Academy of Medical Sciences.

The design and synthesis of new-type superlattices in solid materials are at the frontier of research [1–4]. Such ordered superlattice structure provides an important research environment, where the coupling effect between charge, spin, orbital, and lattice degrees of freedom may extend to new states of matter [5,6]. Especially in perovskite oxides with strongly correlated electron systems, artificial superlattices are capable of exhibiting a wide range of physical and chemical properties, such as ferroelectricity, superconductivity, magnetoresistance, mixed ion/electron conductors, and catalysis [1,7-10]. Therefore, manipulating artificial superlattices is essential to discovering new experimental phenomena.

In the production of perovskite superlattices, physical deposition is the most common and significant procedure currently available [1,10,11]. A significant part of the technology depends on advanced thin-film growth equipment such as pulsed laser deposition (PLD) and molecular beam epitaxy (MBE). In these instruments, the perovskite superlattices can be synthesized by epitaxial growth: unit-cell precise and layer-by-layer [6,12]. These ordered perovskite superlattices, such as $(SrTiO_3)_m$-$(CaTiO_3)_n$, $(SrTiO_3)_m$-$(BaTiO_3)_n$, $(SrTiO_3)_m$-$(PbTiO_3)_n$, $(SrMnO_3)_m$-$(LaMnO_3)_n$, and $(LaMnO_3)_m$-$(SrTiO_3)_n$, displayed much important condensed matter phenomena [1,2,5,9,11,13]. Moreover, other superlattices also show the special coupling effects of electrons and phonons, for example, two-dimensional electron gas of $SrTiO_3/LaAlO_3$ [14], and interfacial charge transfer of $LaMnO_3/SrMnO_3$ [15,16], which opens up an important opportunity for studies on the coupled effect of electrons and phonons. In previous reports, Woodward *et al.* prepared chessboard superlattices and stripes superlattices in double perovskite $NaLaMgWO_6$ and $KLaMnWO_6$ by chemical method [17,18]. After annealing at high temperature with H_2 atmosphere, these metal cations with different ion radii can migrate within the perovskite lattice, as a result of which the perovskite structure can be reconstructed into La-rich and La-poor perovskite unit, leading to the formation of perovskite superlattices. However, in other double perovskite oxides for $Pr_{0.5}Ba_{0.5}MnO_3$, Sr_2MoFeO_6, Sr_2CoWO_6, *etc.*, this regulation method commonly obtains ordered layer-structure perovskite oxides rather than superlattices [10,19-21]. Therefore, it is a great challenge to develop suitable chemical methods to design and tailor unusual perovskite superlattices.

In our previous work, we prepared the 2D ε-MnO_2 nanosheets with ordered Mn vacancy *via* a top-down method, where the Jahn-

* Corresponding author.
E-mail address: shfeng@jlu.edu.cn (S. Feng).

https://doi.org/10.1016/j.cclet.2023.108267
1001-8417/© 2023 Published by Elsevier B.V. on behalf of Chinese Chemical Society and Institute of Materia Medica, Chinese Academy of Medical Sciences.

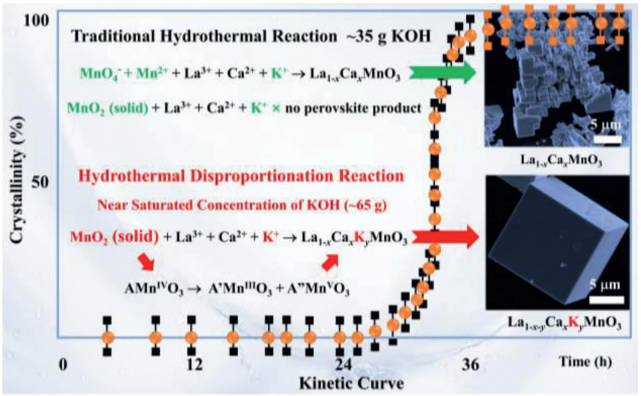

Fig. 1. Synthesis routes, growth kinetic curve and SEM images of perovskite LCMO and LCKMO. Error bar represents systematic and experimental errors.

Teller disproportionation of Mn^{3+} ions in perovskite $La_{0.5}Sr_{0.5}MnO_3$ is the vital step to achieve the delamination of bulk materials and the special superstructure [22]. Under acidic conditions, A-site cations can be dissolved completely, while the Jahn-Teller Mn^{3+} ions generate Mn^{2+} ion in acid solution and Mn^{4+} ions in MnO_2. After undergoing structural reconstruction, a vacancy ordered MnO_2 is formed. Moreover, several studies show that the charge disproportionation in perovskites can create ordered checkerboard structure [23]. The charge order phenomenon in perovskite manganate produces the special magnetoresistance property [24,25]. These studies provide the positive evidence to engineer the superstructure and superlattice through this disproportionation reaction.

Motivated by the above discussions, here we present a new bottom-up method to synthesize a monodispersed perovskite $La_{0.66}Ca_{0.29}K_{0.05}MnO_3$ (LCKMO) with $(LaMnO_3)_1$-$(La_{1-x-y}Ca_xK_yMnO_3)_2$ superlattices by engineering a disproportionation reaction. As opposed to the disproportionation process of Mn^{3+} from perovskite oxide to ordered MnO_2 solids in strong acid, the disproportionation process of $Mn^{4+}O_2$ under strongly alkaline conditions is employed in the manufacturing of perovskite superlattices. Our experiments show that an approximate molten salt system under extreme hydrothermal conditions induces the disproportionation reaction of $Mn^{4+}O_2$ solids and facilitates the doping of three types of A-site cations (*e.g.*, La^{3+}, Ca^{2+} and K^+) in perovskite superlattice. It is well-known that Mn element exists various valence states from Mn^0 to Mn^{7+} and high-valence Mn ion is easy to be stabilized in strong alkaline condition. A strong alkaline condition is also beneficial to the dehydroxylation reaction of hydroxide in the hydrothermal process. Furthermore, K^+ ion can be easily doped into the lattice of perovskite $La_{0.7}Ca_{0.3}MnO_3$ [26]. Therefore, the disproportionation reaction of MnO_2 solids are used to prepare perovskite superstructure. As shown in Fig. 1, MnO_2 solid, $La(NO_3)_3$, $Ca(NO_3)_2$ and 65 g KOH as reagents are used to synthesize perovskite oxide with superlattices. After undergoing the hydrothermal dissolution stage for 24 h, these ions are transported into the growth region to begin hydrothermal crystallization for 48–72 h (Fig. 1). During the first 24-h hydrothermal process, no product is obtained. After 24 h, the target material starts to increase and crystallize. After 40-h hydrothermal reaction, the quality of the product keeps unchanged. After a 72-h hydrothermal reaction, this perovskite LCKMO with superlattices is successfully prepared. To study the effect of KOH on superlattices, perovskite $La_{0.8}Ca_{0.2}MnO_3$ (LCMO) as a reference sample is synthesized *via* a similar method using 25–35 g KOH at 260 °C for 48–72 h. Different from the single cube morphology of prepared LCKMO, the polycrystalline perovskite LCMO is assembled by many staircases' defective cubes (Fig. 1). When the mass of KOH is greater than 65 g, whether the Mn sources are $KMnO_4$ and $MnCl_2$ or a MnO_2, the K^+ ion can be doped into the lattice. However, when the mass of KOH is less than 40 g, K^+ ion cannot be doped into perovskite lattice and MnO_2 solid is not used as raw materials to prepare perovskite oxides under other same reaction conditions (Figs. S1 and S2 in Supporting information). Therefore, the mass of KOH and Mn source are of vital importance to the synthesis of perovskite materials, the doping of K^+ ions, and the regulation of superlattices.

To define the composition of LCMO and LCKMO, inductive coupled plasma emission spectrometer (ICP), SEM-EDS, and XPS are applied. The measured results in Figs. S3 and S4 and Table S1 (Supporting information) show that La, Ca and K elements are doped into the lattice of perovskite LCKMO, whereas K element is not doped in perovskite LCMO. Furthermore, X-ray diffraction (XRD) patterns, high-angle annular dark-field scanning transmitted electron images (HAADF-STEM), and selected area electron diffraction (SAED) patterns are employed to analyze the superstructure. Fig. 2a shows that the XRD patterns of perovskite LCKMO with $(LaMnO_3)_1$-$(La_{1-x-y}Ca_xK_yMnO_3)_2$ superlattices exist many split peaks and diffraction peaks of the superstructure at 5°−20°. Because $LaMnO_3$ and $La_{1-x-y}Ca_xK_yMnO_3$ can be considered as special lattice-matching epitaxial growth, the XRD patterns of perovskite LCKMO display three diffraction peaks in (001) facet, which is similar to epitaxial perovskite thin films [11]. These superstructure diffraction peaks from low angle to high angle can correspond to $(00\frac{1}{3})$, $(0\frac{1}{3}\frac{1}{3})$, $(00\frac{1}{2})$, $(\frac{1}{3}\frac{1}{3}\frac{1}{3})$, $(0\frac{1}{2}\frac{1}{2})$ and $(\frac{1}{2}\frac{1}{2}\frac{1}{2})$, respectively (Fig. 2b). Other diffraction peaks in perovskite LCKMO are index into (001), (011), (111), (002), (012), (112), (022), (013), (003), (113) and (121) of space group *Pm*3*m*, respectively [27]. As shown in Fig. 2c, SAED patterns show consistent results with XRD in superstructure of (001), $(\frac{1}{3}\frac{1}{3}\frac{1}{3})$, $(\frac{1}{2}\frac{1}{2}\frac{1}{2})$ (111) and (112). The double superstructure stems from the A-site ordered structure in $La_{1-x-y}Ca_xK_yMnO_3$. Meanwhile, HAADF-STEM images along the [100] zone axis in Figs. 2d-f confirm the superstructure of (001), $(0\frac{1}{2}\frac{1}{2})$ and $(00\frac{1}{3})$ in perovskite LCKMO. These results clarify the existence of $(LaMnO_3)_1$-$(La_{1-x-y}Ca_xK_yMnO_3)_2$ superlattices, which are similar with $(SrTiO_3)_2$-$(CaTiO_3)_2$ and $(SrMnO_3)_2$-$(LaMnO_3)_1$ superlattices prepared by MBE technology [9,11]. However, perovskite LCMO prepared by traditional method does not show similar superstructure (Fig. S5 in Supporting information).

Atomic-resolution HAADF-STEM image of perovskite LCKMO in Fig. 3a displays the $(LaMnO_3)_1$-$(La_{1-x-y}Ca_xK_yMnO_3)_2$ superlattices and enlarged atomic arrangement image in Fig. 3b shows that there are two rows of green La atoms and one row of ordered green La atom and blue K/Ca atom, indicating the existence of $(LaMnO_3)_1$-$(La_{1-x-y}Ca_xK_yMnO_3)_2$ superlattice. Fig. S6 (Supporting information) also confirms the lattice strains in LCKMO due to the special superlattice, which improves the activity of lattice oxygen (Figs. S7 and S8 in Supporting information) [28,29]. Atomic-scale STEM-EDS elemental mapping in Fig. 3c confirms the above inference about $(LaMnO_3)_1$-$(La_{1-x-y}Ca_xK_yMnO_3)_2$ superlattice. Whereas STEM-EDS elemental mapping of LCMO in Fig. S9 (Supporting information) shows the disordered atomic arrangement in the structure, where La and Ca atoms randomly occupy A site. Because the amount of K ion in LCKMO is very low, it is very difficult to detect K ion at the position in atomic resolution. But ICP, XPS and EDS can demonstrate the existence of K ion, therefore, we further do the corresponding DFT calculations according to the superstructure [30]. Fig. S10 (Supporting information) shows the structural model of perovskite superlattice along the [100] zone axis. To analyze the position of K^+ ion in perovskite superlattices and simplify this calculation, we only calculate the energy profile in different substitute positions of perovskite superlattices (Fig. S10). Energies and formation energies of the three superstructures (Fig. S10d) show that the

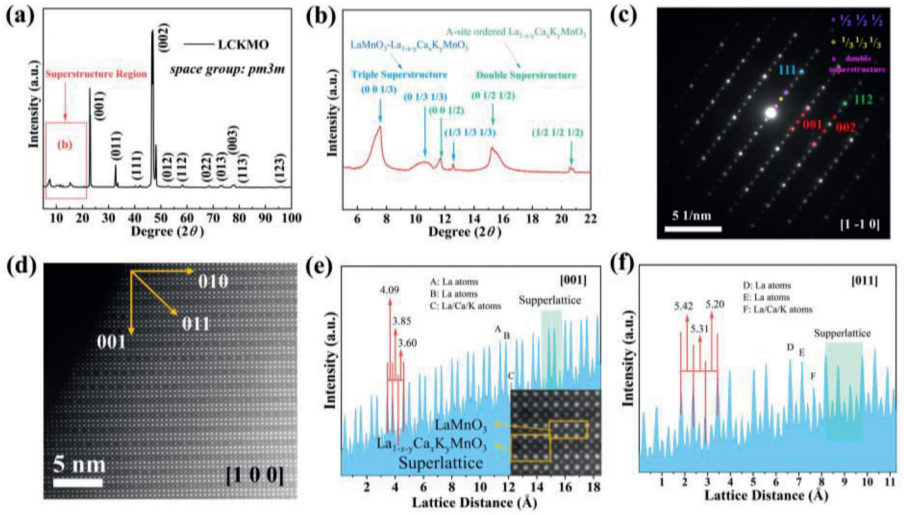

Fig. 2. Crystal structure and atomic scale superlattices of perovskite LCKMO. (a) X-ray diffraction (XRD) patterns of perovskite $La_{0.66}Ca_{0.29}K_{0.05}MnO_3$. (b) Enlarge image for XRD at the 2θ degree of 5°−22°. (c) SAED patterns along [1$\bar{1}$0] zone axis and (d) atomic-resolution HAADF-STEM images along [100] zone axis for perovskite LCKMO with $(LaMnO_3)_1$-$(La_{1-x-y}Ca_xK_yMnO_3)_2$ superlattice. Intensity profile across the LCKMO measured from (e) crystal facet (001) and (f) crystal facet (011) in (d). The distance between two intensities matches with the separation between crystal facets. A and D represent La atom in $LaMnO_3$, B and E represent La atom in $La_{1-x-y}Ca_xK_yMnO_3$, C and F represent La/Ca/K atom $La_{1-x-y}Ca_xK_yMnO_3$.

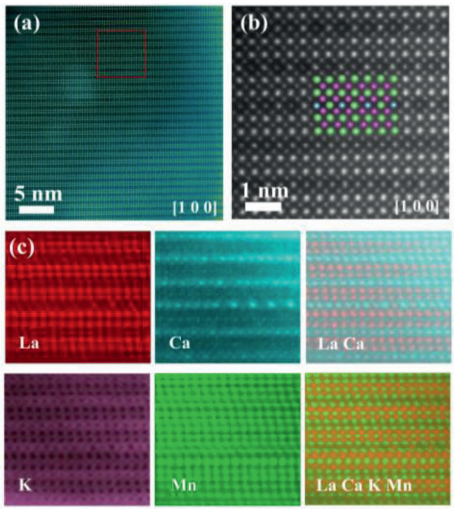

Fig. 3. Atomic-scale elemental mapping and atomic arrangement of perovskite LCKMO. (a) Atomic-resolution HAADF-STEM image of $(LaMnO_3)_1$-$(La_{1-x-y}Ca_xK_yMnO_3)_2$ superlattices along [100] zone axis. (b) Enlarged atomic arrangement image in red area of (a), where green sphere represents La atom, blue sphere represents Ca/K atom, and pink sphere represents Mn atom. (c) Atomic resolution STEM-EDS chemical mapping of perovskite LCKMO for La, Ca, K and Mn elements.

structure of K → Ca possessed the lowest matter energy and the lowest formation energy compared to 0% K and K → La, indicating that a small amount of K^+ ions is doped in the Ca site of the superstructure. Finally, to further determine the position of oxygen ions, atomic-scale STEM-EDS elemental mapping about oxygen elements is also measured. It has been observed that STEM-EDS element mapping in Figs. S11d-f (Supporting information) is consistent with the atomic arrangement of the structural model (Figs. S11a-c in Supporting information). By this method, the position of oxygen ions can be better determined.

Previously, we found that the perovskite LCKMO showed a better p-n junction effect at the atomic scale [27]. But its structure and synthesis principle keep elusive. Therefore, in this work, we study the superlattice structure, electronic structure, and synthetic principle and try to analyze the reasons for the p-n junction phenomenon. Perovskite LCMO as a reference sample does not show related electronic property and similar superlattices. Ca L-edge XAS spectra in Fig. S12a (Supporting information) show that LCKMO contains more Ca elements on the surface due to strong white line peak. In O K-edge XAS spectra (Fig. 4a), it has been observed that peak a in perovskite LCKMO shifts to lower energy compared to LMO and LCMO. This result indicates that local Mn^{5+} ion may exist in perovskite LCKMO and produces a vacancy in 3d $t_{2g}{}^2$ orbital, which leads to the decrease of Mn 3d orbital energy in local structure [31]. Furthermore, the separation between peak a and peak b in LCKMO is a little wider than LCMO, CMO and LMO (Fig. S13 in Supporting information), which indicates that high oxidation-state Mn ion enhances the transition of Mn 2p → 3d $e_g\uparrow$ in MnO_6 octahedron and facilitates the splitting of hybrid orbitals. Mn^{5+} ion in typical superlattices may be stabilized by optimizing the hybrid orbitals between Mn 3d and O 2p or charge disproportionation [32,33]. Mn L-edge XAS spectra in Fig. 4b shows that LCKMO has a higher average oxidation state for Mn atom than LCMO and LMO because the energy position of peaks A and B shifts to higher binding energy from LMO, LCMO, CMO to LCKMO. Therefore, the superstructure in LCKMO may contain various Mn ions with different chemical environments (*e.g.*, La^{3+}, Ca^{2+} and K^+), which is stabilized by tuning the hybrid orbitals between Mn 3d and O 2p [34,35]. Fig. S12b (Supporting information) shows the atomic arrangement in the superlattices and local p-n junction model. We can see that these atoms in the red remark section display different contrast in color, which stems from that atom column in A site contains a different concentration of La, Ca and K. Different A-site atoms in LCKMO can produce the different electronic configuration of B site atom, which may induce a local p-n junction and magnetic property (Fig. S14 in Supporting information).

To illustrate the local electronic structure in superlattices [13,36,37], atomic-resolution EELS spectra of LCKMO and LCMO are performed. Figs. 4c and d display that the selected Mn atom column possesses a different electronic state in Mn L-edge EELS spectra of LCKMO, where their white line peak position has distinct change. This result indicates that the different electron density of Mn atoms in the different atomic columns stems from different A-

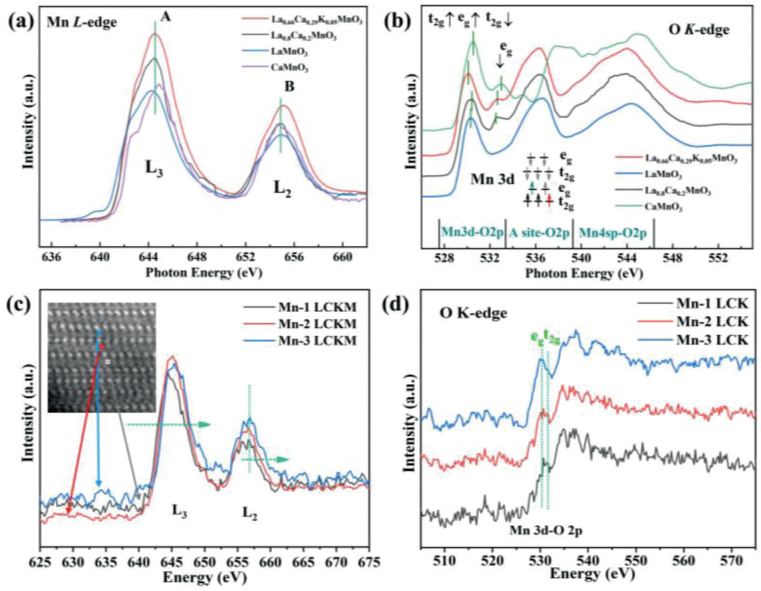

Fig. 4. (a) O K-edge and (b) Mn L-edge X-ray absorption spectrum of $LaMnO_3$, $La_{0.8}Ca_{0.2}MnO_3$ and $La_{0.66}Ca_{0.29}K_{0.05}MnO_3$. (c) Atomic-scale Mn L-edge electron energy loss spectroscopy (EELS) simultaneously recorded *via* atomic-resolved EELS mapping found by HAADF-STEM mode along [100] (Fig. 3). (d) The corresponding O K-edge EELS spectra in the three-position of perovskite LCKMO. These shown spectra were obtained using a window corresponding to the sum of four pixels.

site environments. Furthermore, we also calculate the corresponding integral area of Mn L_3/Mn L_2 to confirm the electron density of the Mn atom. Fig. S15 (Supporting information) demonstrates that Mn-1 displays a higher ratio of Mn L_3/Mn L_2, which suggests that Mn-1 possesses more electrons in 3d orbitals than Mn-2 and Mn-3, which is consistent with the above conclusion obtained by the change of peak position. As displayed in Fig. 4d, the hybridization between Mn 3d and O 2p is different for these three samples in peak position and e_g/t_{2g} ratio. Whereas Mn L-edge and O K-edge EELS spectrum of perovskite LCMO (Fig. S16 in Supporting information) in different positions show the same results. Based on these data, we can infer that perovskite LCKMO with superlattices exists three different Mn atoms. Of course, some further explanations about this material and novel electricity phenomenon need to be explored in the future.

In summary, we report a novel bottom-up method to engineer perovskite superlattices, where a monodispersed perovskite LCKMO with $(LaMnO_3)_1$-$(La_{1-x-y}Ca_xK_yMnO_3)_2$ superlattices is synthesized. The special superlattices are demonstrated by various characterizations, such as SAED, HAADF-STEM, XRD, and atomic-resolution STEM-EDS elemental mapping. A near-saturated concentration of KOH solution is crucial for tailoring perovskite superlattices. When the mass of KOH is less than 35 g, we only obtain the disordered polycrystalline perovskite LCMO without K^+ ion, which suggests that the disproportionation reaction of MnO_2 solids induced by the extreme hydrothermal condition is a key step to form the ordered superlattice. Furthermore, the atomic resolution EELS spectrum confirms the three different manganese atoms in superlattices, which were attributed to cations at the A-site with different valence states (*e.g.*, La^{3+}, Ca^{2+} and K^+). This study not only provides an important platform for engineering atomic scale superlattices, but also highlights the importance of oxide superlattices design in obtaining new states of condensed matter that exhibits special experimental phenomena and functional properties.

Declaration of competing interest

The authors declare that they have no financial and personal relationships with other people or organizations that can inappropriately influence the work.

Acknowledgments

We thank Professor Lin Gu and Professor Qinghua Zhang for helpful measurements using a spherical aberration correction electron microscope. This work was supported by National Natural Science Foundation of China (Nos. 21831003, 21801090 and 22293041), China Postdoctoral Science Foundation (No. 2019M661203), and Users with Excellence Program of Hefei Science Center CAS (No. 2020HSC-UE002). The authors thank beamlines MCD-A and MCD-B (Soochow Beamline for Energy Materials) in National Synchrotron Radiation Laboratory for providing beam time. The calculations have been performed using the Vienna ab-initio simulation package VASP.6.1.0.

Supplementary materials

Supplementary material associated with this article can be found, in the online version, at doi:10.1016/j.cclet.2023.108267.

References

[1] A.K. Yadav, C.T. Nelson, S.L. Hsu, et al., Nature 530 (2016) 198–201.
[2] V.A. Stoica, N. Laanait, C. Dai, et al., Nat. Mater. 18 (2019) 377–383.
[3] Y.L. Tang, Y.L. Zhu, X.L. Ma, et al., Science 348 (2015) 547–551.
[4] S. Das, Y.L. Tang, Z. Hong, et al., Nature 568 (2019) 368–372.
[5] A.R. Damodaran, J.D. Clarkson, Z. Hong, et al., Nat. Mater. 16 (2017) 1003–1009.
[6] E. Maniv, R.A. Murphy, S.C. Haley, et al., Nat. Phys. 17 (2021) 525–530.
[7] N. Driza, S. Blanco-Canosa, M. Bakr, et al., Nat. Mater. 11 (2012) 675–681.
[8] E. Bousquet, M. Dawber, N. Stucki, et al., Nature 452 (2008) 732–736.
[9] J. Ravichandran, A.K. Yadav, R. Cheaito, et al., Nat. Mater. 13 (2014) 168–172.
[10] S. Sengodan, S. Choi, A. Jun, et al., Nat. Mater. 14 (2015) 205–209.
[11] S.J. May, P.J. Ryan, J.L. Robertson, et al., Nat. Mater. 8 (2009) 892–897.
[12] Y.J. Wang, Y.P. Feng, Y.L. Zhu, et al., Nat. Mater. 19 (2020) 881–886.
[13] M. Li, C. Tang, T.R. Paudel, et al., Adv. Mater. 31 (2019) e1901386.
[14] A. Ohtomo, H.Y. Hwang, Nature 427 (2004) 423–426.
[15] A. Bhattacharya, S.J. May, S.G.E. te Velthuis, et al., Phys. Rev. Lett. 100 (2008) 257203.
[16] H. Yamada, P.H. Xiang, A. Sawa, Phys. Rev. B 81 (2010) 014410.
[17] S. García-Martín, E. Urones-Garrote, M.C. Knapp, et al., J. Am. Chem. Soc. 130 (2008) 15028–15037.
[18] S. Garcia-Martin, G. King, E. Urones-Garrote, et al., Chem. Mater. 23 (2011) 163–170.
[19] N.I. Kim, Y.J. Sa, T.S. Yoo, et al., Sci. Adv. 4 (2018) eaap9360.
[20] M.C. Viola, M.J. Martínez-Lope, J.A. Alonso, et al., Chem. Mater. 15 (2003) 1655–1663.

[21] T. Shimada, J. Nakamura, T. Motohashi, et al., Chem. Mater. 15 (2003) 4494–4497.
[22] Y.L. Jiang, L. Yuan, X.Y. Wang, et al., Angew. Chem. Int. Ed. 59 (2020) 22659–22666.
[23] Y. Hosaka, N. Ichikawa, T. Saito, et al., J. Am. Chem. Soc. 137 (2015) 7468–7473.
[24] D. Bhattacharya, H.S. Maiti, Phys. Rev. B 66 (2002) 132413.
[25] M.E. Brown, A.H. Bouchez, C.A. Griffith, et al., Nature 420 (2002) 795–797.
[26] C. Chen, F. Yu, N. Xu, D. Fan, Ceram. Int. 46 (2020) 15646–15653.
[27] S. Feng, H. Yuan, Z. Shi, et al., J. Mater. Sci. 43 (2007) 2131–2137.
[28] D. Guan, G. Ryu, Z. Hu, et al., Nat. Commun. 11 (2020) 3376.
[29] D. Guan, J. Zhong, H. Xu, et al., Appl. Phys. Rev. 9 (2022) 011422.
[30] J. Qian, Q. Guo, L. Liu, J. Mater. Chem. A 5 (2017) 16786–16795.
[31] D. Sherman, Am. Miner. 69 (1984) 788–799.
[32] J. Miao, J. Li, J. Dai, et al., Ind. Eng. Chem. Res. 59 (2019) 99–109.
[33] D. Guan, J. Zhou, Z. Hu, et al., Adv. Funct. Mater. 29 (2019) 1900704.
[34] H. Wu, T. Burnus, Z. Hu, et al., Phys. Rev. Lett. 102 (2009) 026404.
[35] Y. Shen, Y. Zhu, J. Sunarso, et al., Chemistry 24 (2018) 6950–6957.
[36] A. Gulec, D. Phelan, C. Leighton, R.F. Klie, ACS Nano 10 (2016) 938–947.
[37] R. Cortes-Gil, M.L. Ruiz-Gonzalez, D. Gonzalez-Merchante, et al., Nano Lett. 16 (2016) 760–765.